# Design for Approaching Cicada-Wing Reflectance in Low- and High-Index Biomimetic Nanostructures

**Yi-Fan Huang,[†] Yi-Jun Jen,[‡] Li-Chyong Chen,[§] Kuei-Hsien Chen,[*,§,∥] and Surojit Chattopadhyay[*,†,⊥]**

[†]Institute of Biophotonics, National Yang-Ming University, Taipei 112, Taiwan, [‡]Department of Electro-Optical Engineering, National Taipei University of Technology, Taipei 106, Taiwan, [§]Center for Condensed Matter Sciences, National Taiwan University, Taipei 106, Taiwan, [∥]Institute of Atomic and Molecular Sciences, Academia Sinica, Taipei 106, Taiwan, and [⊥]Biophotonics and Molecular Imaging Research Center, National Yang Ming University, Taipei 112, Taiwan

**ABSTRACT** Natural nanostructures in low refractive index Cicada wings demonstrate ≤1% reflectance over the visible spectrum. We provide design parameters for Cicada-wing-inspired nanotip arrays as efficient light harvesters over a 300−1000 nm spectrum and up to 60° angle of incidence in both low-index, such as silica and indium tin oxide, and high-index, such as silicon and germanium, photovoltaic materials. Biomimicry of the Cicada wing design, demonstrating gradient index, onto these material surfaces, either by real electron cyclotron resonance microwave plasma processing or by modeling, was carried out to achieve a target reflectance of ∼1%. Design parameters of spacing/wavelength and length/spacing fitted into a finite difference time domain model could simulate the experimental reflectance values observed in real silicon and germanium or in model silica and indium tin oxide nanotip arrays. A theoretical mapping of the length/spacing and spacing/wavelength space over varied refractive index materials predicts that lengths of ∼1.5 μm and spacings of ∼200 nm in high-index and lengths of ∼200−600 nm and spacings of ∼100−400 nm in low-index materials would exhibit ≤1% target reflectance and ∼99% optical absorption over the entire UV−vis region and angle of incidence up to 60°.

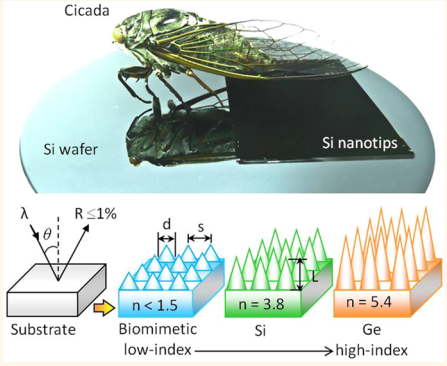


**KEYWORDS:** biomimetic nanostructures · Cicada wing · antireflection · photonic · gradient index · photovoltaic · finite difference time domain

The expression of complementary electronic and optical properties is key to the performance of optoelectronic devices. While intrinsic material quality controls the electronics, light harvesting through the control of reflectance in materials with varying refractive indices (RI) controls the optical performance.[1−5] Different materials and optical principles have been investigated to achieve extremely high absorption (A) or antireflection (AR) over select frequency bands. These include an ultrathin stack of tilted graphene sheets,[6,7] plasmonic nanoparticles or metamaterial structures that utilize optical resonance/scattering/trapping,[8−11] extra-long vertically aligned carbon nanotubes,[12,13] subwavelength structures,[14] and Mie resonators.[15,16] In spite of such impressive properties demonstrated by these new materials, the industry can only use the relatively inferior dielectric thin film stack AR coatings[17] and chemically etched pyramidal structures because these new technologies are still in their infancy due to the lack of a simple design recipe that could be applied universally and independent of substrate RI.

Biomimetic nanostructures,[18−20] demonstrating gradient index of refraction (GRIN), have shown ultralow AR properties for photovoltaics (PV),[21,22] photoelectrochemical,[23] triboelectric energy,[24] photodetectors,[25] and bactericidal[26] applications. Material-specific biomimetic AR structures have been designed to work over a broad band and over a wide angle of incidence (AOI).[1,27−32] These materials may or may not cater to the varied needs of the application industry such as PV. In addition, the absolute value of the highest absorption (lowest reflection) may be technically irrelevant since photoelectronic conversion in the devices, mentioned above, is not sensitive enough to account for <0.5−1% changes in absorption/reflectance.

* Address correspondence to sur@ym.edu.tw, chenkh@pub.iams.sinica.edu.tw.

Received for review August 25, 2014 and accepted January 2, 2015.

**Published online January 02, 2015**
**10.1021/nn506401h**

However, nearly tens of micrometers deep surface texturization is required to achieve ultrahigh (~99%) absorption, which is not the objective of this research.[12,13,15] Such long nanostructures impose a heavy burden on the device fabrication procedures, involving etching time and severely deteriorating the electronic quality through defect recombination of the material. Extreme AR values, such as $R \sim 0.045\%$,[12] are prohibitive and useless for practical devices. As a solution, nature has demonstrated efficient absorber structures in Cicada wings and moth eyes[33,34] on much smaller length scales. In fact, the best PV cells require only about $R \sim 1\%$ from its surface to complement the required electronic properties.[2,21] Hence, instead of a technically useless ultrasmall $R$ value, we should focus more on the efficiency of $R$ suppression per unit length ($L$) or spacing ($S$) or both of the nanostructures. Rationally, (i) specifically designed, (ii) shortest possible nanostructures to achieve (iii) a target $R$% (~1%), (iv) over the full visible spectrum (~400−800 nm), (v) over a reasonably broad AOI (0−60°), and (vi) on different RI substrates would result in significant cost reduction. There are some reports that partially address the above issues, such as control of $R$ as a function of $L$ or $S$.[35,36] The issues of broad band and wide AOI AR have been addressed either individually or in totality but in a specific material with specific dimensions.[28−32,35,36] However, it is crucial to determine a recipe with optimum $L$ and $S$ of these light-harvesting structures to arrive at a design principle that would address all six requirements mentioned above. Such design principles are not available that can be adopted directly from the journal to the floors of the production line.

To meet the above-mentioned criteria, as numbered from i to vi, in this article, we report the fabrication of (i) Cicada-inspired (specifically designed) AR nanostructure arrays on silicon (Si) and germanium (Ge) and model these using finite difference time domain (FDTD) calculations using (ii) the $L$ and the $S$ as the fitting parameters. The model can then be used on other materials such as silica ($SiO_2$) and indium tin oxide (ITO), in addition to Si and Ge, to map and predict the smallest $L$ and $S$ to achieve the (iii) target $R \sim 1\%$ over the (iv) 400−800 nm spectrum and (v) 0−60° AOI for (vi) PV materials having different RI.

## RESULTS

Nature makes use of submicron structures on biological surfaces in order to achieve unmatched optical effects. In this article, we have selected one such natural photonic structure, namely, the Cicada wing, to study its reflective properties and use it for designing artificial structures suitable for optoelectronic devices. Figure 1a shows the photograph of an adult Cicada (collected dead in summer 2014) sitting on a highly reflective polished planar silicon wafer and a

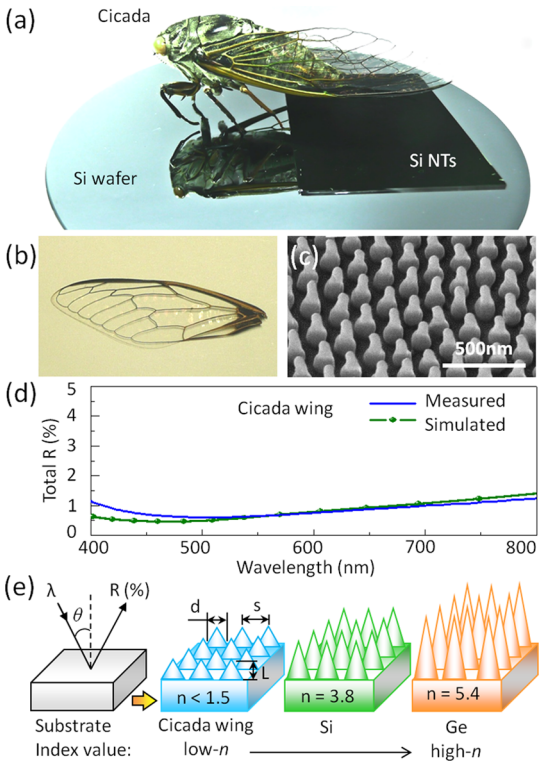


**Figure 1. Antireflective nanostructure arrays on transparent cicada wing. (a) Photographic image of a Cicada specimen placed partially on a polished silicon wafer and on a piece of SiNTs (size 4 cm × 5 cm). (b) Photographic image, (c) tilted top view SEM image, and (d) measured and simulated total hemispherical reflectance (total $R$%) spectrum as a function of wavelength for the Cicada wing. (e) Left to right: Schematic representation of reflectance reduction, compared to planar surfaces, in real and index-controlled biomimetic nanostructures with feature parameters of $d$ (diameter), $S$ (spacing), and $L$ (length) in material with variable bulk refractive index ($n$, at 633 nm). Abbreviations used: $\lambda$, incident wavelength; $\theta$, angle of incidence; Si, silicon; Ge, germanium.**

dark nanostructured Si surface, which we will discuss later. Evidently, the polished Si reflects the image of the Cicada on the left-hand side of the image. However, the dark piece of nanostructured Si sample (size 4 cm × 5 cm) with biomimetic architecture does not reflect the image of the Cicada at all. This is a simple visual comparison of the AR properties of the polished wafer and the nanostructured Si surface. The adult Cicada wing is transparent, excluding some small parts of the wing edge and fibrous support network, as shown in Figure 1b. The scanning electron microscopy (SEM) image reveals highly ordered array of nanosized protuberances on its surface. The conical structures, hereafter to be called nanotips (NTs), are ~250 nm tall and arranged in a hexagonal array with a center-to-center distance of ~150 nm (Figure 1c). The morphology of the Cicada wing is very similar to the corneal nipple arrays found in moths,[33] and the transparent wing of *Cephonodes hylas*[34,37] has been described to have good AR surfaces.[38,39] In order to verify the AR property of the wing NT array, we have studied the total

(specular + diffuse) hemispherical reflectance within the wavelength region from 400 to 800 nm with an integral sphere attached to the measurement system. The Cicada wing showed a very low reflectivity of ~1% in the visible wavelength (Figure 1d), and we set this as our target reflectance for the biomimetic nanostructures we are going to generate. This low reflectivity could be simulated (Figure 1d) through the FDTD calculations with a model nanostructure using RI values of the wing material chitin (Supporting Information Figure S1). The SiNT shown in Figure 1a had nanostructures resembling those of the Cicada wing. Compared to the flat surfaces, these NT arrays would certainly show reduced reflectance. However, we were curious if the morphology (length, spacing) of these NT arrays need to be controlled to achieve a practically meaningful target reflectance when we translate this design to real material surfaces used in photovoltaics or light-harvesting devices having varied RI (Figure 1e).

Translation of the Cicada wing design in a variety of synthetic material surfaces must also demonstrate similar AR and light-harvesting properties over a broad band. Not only that, a proper choice of material suiting the particular application is also required. Scanning the entire wavelength and the material spectrum with the given natural design is difficult experimentally. Therefore, we took to theoretical modeling and calculations. We have demonstrated previously that SiNTs are efficient antireflectors in the visible and near-infrared wavelength zone[15] compared to nanowires or nanorods with dual diameter.[40] Those studies were mostly done to achieve the lowest reflectance with no restriction on the geometry dimension and hence being indifferent to the electronic properties. Here, we have performed numerical calculations to simulate the 1% target reflectance for light-harvesting nanostructures in varied RI media.[41] We have chosen $SiO_2$, ITO, Si, and Ge that demonstrate a spectrum of RI values and have been used in devices such as solar cells and photodetectors.

Basic principles of subwavelength structures predict a decrease in reflectance as $L$ increases with $S < \lambda$.[1,38,39] This motivates us to study the variation of the geometrical factors ($L/S$ and $S/\lambda$, with $S \leq \lambda$) of the NT and predict an efficient AR architecture. AR efficiency of the design is not the minimization of the absolute reflectance value, but the rate at which it decreases as a function of the geometrical parameters $L/S$ and $S/\lambda$ in the selected spectral region. The answer to this question is provided by the simulation results presented in Figure 2 for nanostructures with different RI and AOI = 0°.

Over a broad band (300−1200 nm), the $R$% decreased as $L/S$ is increased at a fixed value of $S/\lambda$ for SiNTs (Figure 2a). Similarly, for sufficiently long SiNTs ($L/S \sim 3$), $R$% is suppressed as $S/\lambda$ increases to 1 (Figure 2b). From Figure 2a,b, it is easy to demonstrate the rate of decrease in $R$% as a function of either $L/S$ (Figure 2c) or $S/\lambda$ (Figure 2d) at a set wavelength of 500 nm at which the Cicada wing showed a minimum $R \sim 0.6\%$ (Figure 1d). Similar plots for other materials ($SiO_2$, ITO, Si, Ge) could also be generated (Figure 2c,d) from the data shown in Supporting Information Figure S2. The results show a decrease in $R$% as $L/S$ is increased for these materials, and $R$% approaches ~1% when $L/S = 1$ for $SiO_2$. An increasing RI of the material would increase the required $L/S$ to achieve the target reflectance. The results of Figure 2d show a decrease in $R$% as $S/\lambda$ is increased for these materials, and $R$% approaches ~1% when $S/\lambda = 0.1$ for $SiO_2$. An increasing RI of the material would increase the required $S/\lambda$ to achieve the target reflectance.

Next, in order to predict the best NT geometry for the target reflectance, we systematically calculated the reflectance spectrum by varying $S/\lambda$ and $L/S$ independently in our simulations. For instance, the reflectance values of $SiO_2$NT were plotted as a function of each $S/\lambda$ and $L/S$ combination at $\lambda = 500$ nm to obtain a 3D graph (Figure 2e). The same strategy was employed subsequently for ITO (Figure 2f), Si (Figure 2g), and Ge (Figure 2h). The $S/\lambda$ was changed from 0 to 1, and $L/S$ was changed from 0 to 4 for $SiO_2$/ITO and from 0 to 6 for Si/Ge. These results reveal that the AR property correlates consistently with the $S/\lambda$ and $L/S$ of the NTs. The 3D reflectance map shows a half-cup shape with a purple valley and multicolored slopes. From the $R$% scale bar in the case of $SiO_2$, the purple color represent $R \leq 1\%$, whereas the other colors represent $R > 1\%$ (Figure 2e). These plots clearly show at which values of $L/S$ and $S/\lambda$, $R < 1\%$ could be achieved on $SiO_2$ (Figure 2e), ITO (Figure 2f), SiNT (Figure 2g), and GeNT (Figure 2h) structures at 500 nm. Instead of a 3D plot, the result is presented in a 2D format to know the precise values of $L/S$ and $S/\lambda$ that would result in the target reflectance (Supporting Information Figure S2). For an efficient AR, there is no need to go deeper into the purple valleys (meaning high $L/S$ and $S/\lambda$), and the smallest possible value of these indicators ($L/S$ and $S/\lambda$) could be selected from within the purple zone for ease of fabrication and retention of good electronic quality. Reflectance plots in Figure 2 thus provide an AR design rule to suit specific manufacturing techniques for light harvesting and penetration (transmission) in materials within those described.

For any solar energy harvesting material, the ability to collect light from a wide AOI is another critical factor that we must consider in addition to the broad-band nature of the AR property. Figure 3 shows the calculated specular reflectance of random (Figure 3a), s-polarized (Figure 3b), and p-polarized (Figure 3c) light as a function of AOI for varied length of SiNTs with a fixed $S = 250$ at 633 nm. Results for the planar Si are also presented for comparison.

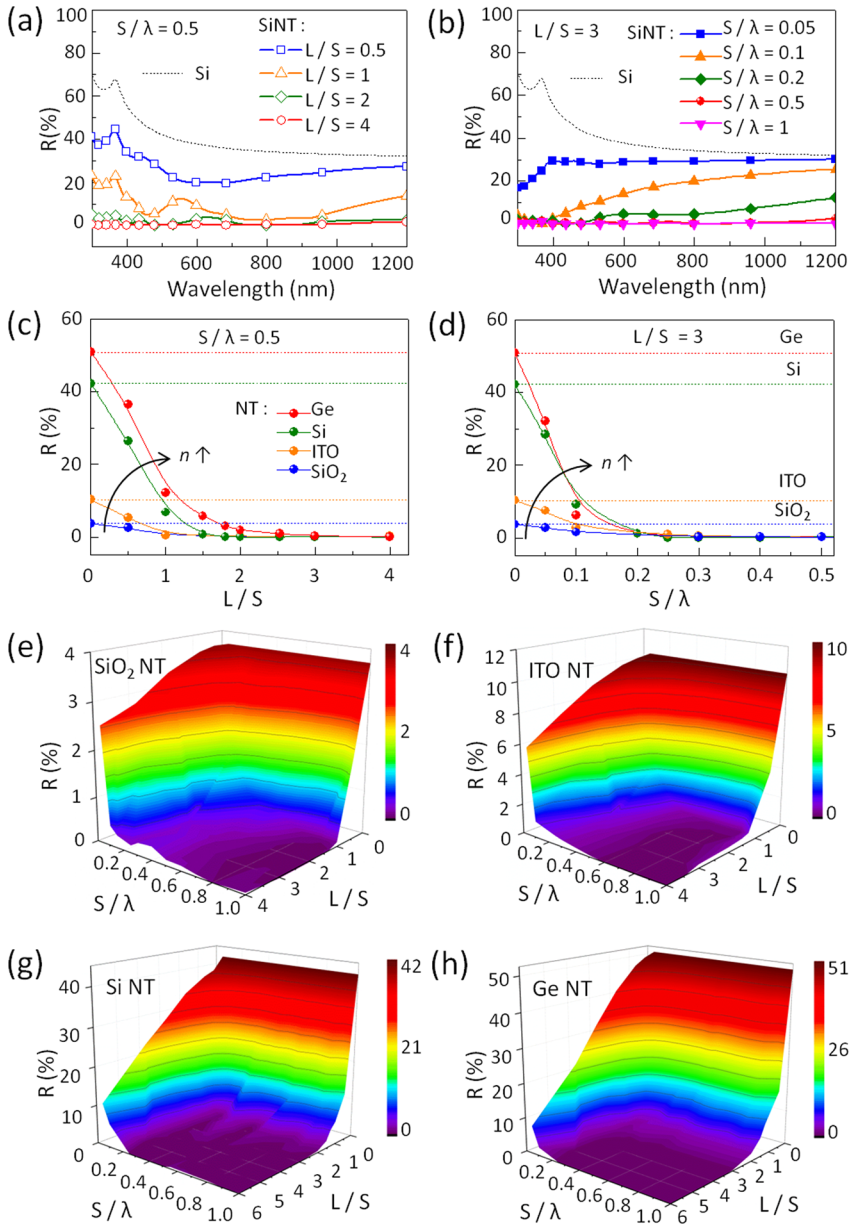


**Figure 2. Calculated broad band antireflection property of Cicada mimetic nanotip arrays. Simulated reflectance as a function of the wavelength for SiNTs (a) with varying $L/S$ at a fixed $S/\lambda = 0.5$ and (b) with varying $S/\lambda$ at a fixed $L/S = 3.0$. Simulated reflectance as a function of the geometrical parameters for different RI substrates (low-index $SiO_2$; medium-index ITO; high-index Si and Ge) at a specific wavelength of 500 nm (c) as a function of $L/S$ with fixed $S/\lambda = 0.5$, and (d) as a function of $S/\lambda$ with fixed $L/S = 3$. Dashed lines indicate the reflectance values (at 500 nm) for the planar polished wafer (blue, $SiO_2$; orange, ITO; green, Si; red, Ge) as reference. The solid lines connecting the data points are a guide to the eye only. The solid arrow indicates increasing index of the materials used. Simulated 3D reflectance ($R$%) map on the NTs as a function of $L/S$ and $S/\lambda$ for different refractive index substrates: (e) $SiO_2$ NT; (f) ITO NT; (g) SiNT, and (h) GeNT. Gradient spectral colors from red to purple represent the maximum and minimum reflectance values for the NT. $L$ and $S$ represent length and spacing of the nanotip array, respectively.**

Generally, at normal incidence, the degree of polarization is irrelevant. However, the reflectance of planar Si strongly depends on both AOI and polarization of the incident light, which can be predicted by the Fresnel equations for a smooth surface. In contrast, the calculated reflectance of the SiNTs shows remarkable insensitivity to both AOI and polarization of the incident light. The angle-resolved reflectivity of SiNTs is strongly reduced with increasing $L$ from 125 to 2000 nm. For SiNTs, $R \sim 1\%$ can be achieved over AOI $\leq 60°$ with $L \geq 1000$ nm, leading to the so-called omnidirectional AR (Figure 3a–c). The $R$% for s-polarized light decreases monotonically with increasing $L$ at all AOI (Figure 3b). A similar reduction phenomenon was observed for the p-polarized light for AOI below 60°, but the reflectance increased for AOI > 70 ° (Brewster's angle) (Figure 3c).

A 3D plot can now be presented to show the variation of $R$% as a function of the $L$ and $S$ of the $SiO_2$ (Figure 3d), ITO (Figure 3e), SiNT (Figure 3f), and

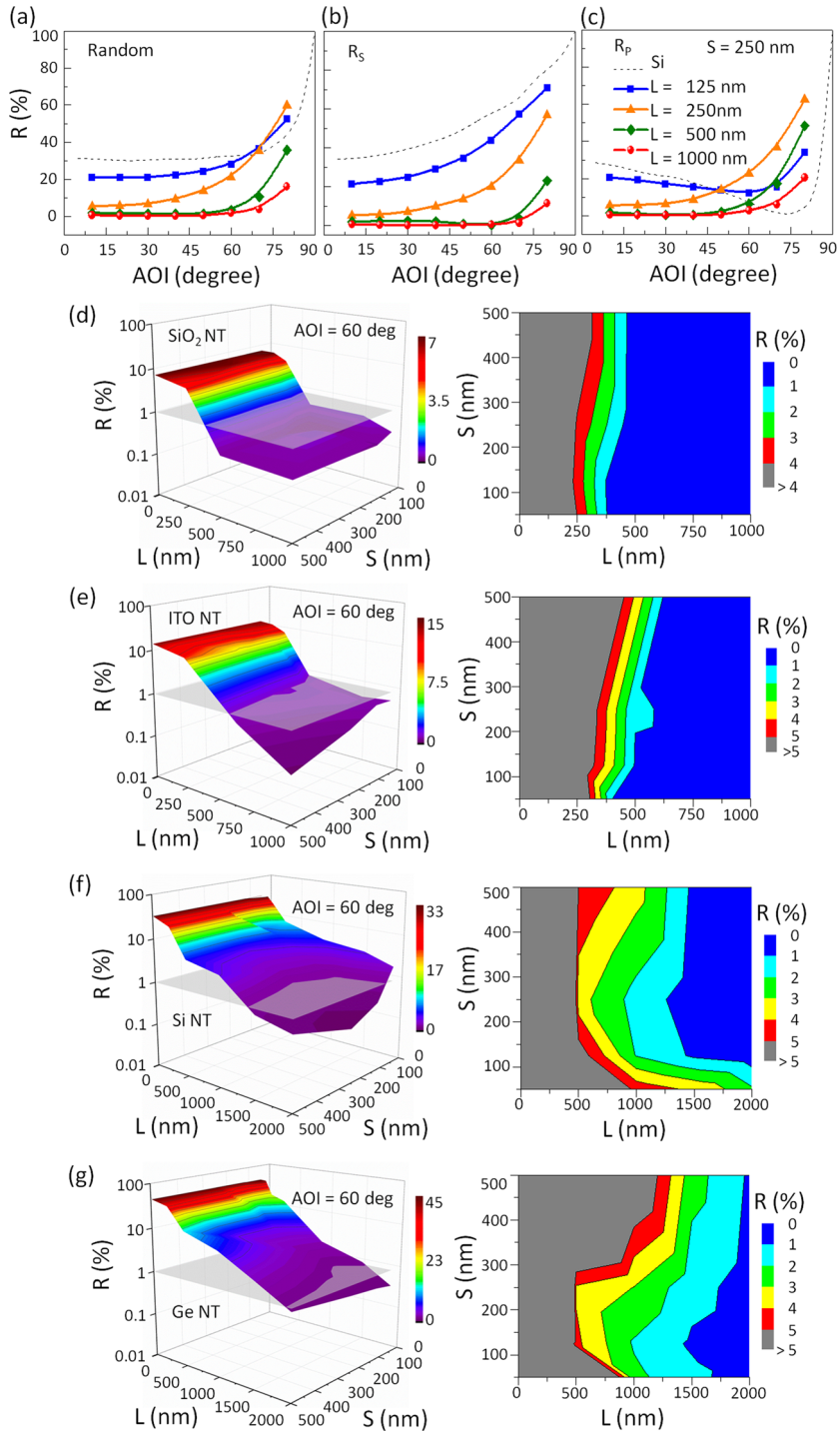


**Figure 3. Calculated wide-angle antireflection property of cicada mimetic nanotip arrays. Simulated reflectivity as a function of AOI for SiNTs at a fixed spacing $S$ = 250 nm and increasing length $L$ from 125 to 1000 nm, with (a) random, (b) s-polarized, and (c) p-polarized 633 nm incident beam. The dashed lines indicate the reflectance values for the planar polished silicon wafer (reference). The 3D plot of reflectance (at 633 nm and 60° AOI) as a function of $L$ and $S$ is shown for cicada mimetic (d) $SiO_2$, (e) ITO, (f) Si, and (g) Ge nanotip structures in the left-hand column. A plane has been drawn at the target reflectance of 1% in each of these plots (d−g) to indicate which $L$ and $S$ values are at or below this plane (1% reflectance value) for the particular material. The right-hand column shows a 2D projection of the corresponding 3D reflectance data (shown on the left-hand side) with a different $R$% scale to distinguish smaller changes in reflectance as a function of $L$ and $S$.**

GeNT (Figure 3g) arrays at a particular AOI = 60°. By defining a plane at which $R$ = 1% and allowing it to intersect the resulting 3D plot, we can generate areas with $L$ and $S$ values that would result in $R \leq 1\%$ for materials with different RI at AOI = 60°. Clearly, as the RI increased, the area of the $L \times S$ space, for $R \leq 1\%$, shifted to longer values of $L$ and smaller values of $S$. This could be understood better by looking at the 2D plot

presented in the right column of Figure 3d–g. The data used for the generation of Figure 3d–g (for different material) can be found in Supporting Information Figure S3 (Si), Figure S4 ($SiO_2$), Figure S5 (ITO), and Figure S6 (Ge). Figures S3–S6 also contain additional data for AOI = 30 and 80°.

Once we know, by calculations, about the morphology dimensions of different types of biomimetic NT arrays demonstrating AR properties, it is now time to show its fabrication in the laboratory. To translate the natural AR design of the Cicada wing on Si and Ge, we used a top-down plasma etching process. The schematic illustration of the fabrication procedure is shown in Figure 4a. The Si and Ge wafers were plasma-etched in a high-density electron cyclotron resonance plasma reactor (Figure 4a) using random nanomasks of silicon carbide generated *in situ* in the plasma.[42,43] Arrays of random NT structures, with tapered apexes, were prepared with a length that could be controlled as a function of etching time and gas flow ratios. Compared to the planar substrate–air interface with abrupt or ungraded RI (Figure 4b), the NTs demonstrate a graded RI (Figure 4c) because the volume fraction of the wafer material (Si or Ge) increased slowly as we move deeper. The morphology and dimension of the nanostructures would dictate how smooth the transition of the RI from air to the bulk substrate would be. The detailed geometrical information on the NTs was examined by SEM for Si (Figure 4d–h) and Ge (Figure 4i–m). The results are summarized in Table 1 for different nanotip arrays. The SEM images confirm the subwavelength (sub-$\lambda$) dimensions for the diameter and spacing of the nanostructures, nearly matching those in the Cicada wings.

After the fabrication of the SiNT and GeNT arrays, we had to measure their AR properties first as a function of wavelength and then with AOI to verify if the theoretical predictions could be corroborated. A visual inspection of the materials, presented by optical photographs, compare how the reflective as-purchased wafers turned into highly absorbing dark materials after the plasma processing (Figure 5a,b). The results of total hemispherical reflectance (Figure 5c,d) and total hemispherical absorption (Figure 5e,f) properties for different lengths of SiNT and GeNT surfaces are compared in the UV–vis–NIR region at normal incidence. In general, both polished Si and Ge surfaces showed high Fresnel reflection of 40–80%, due to their high RI.[41] The reflectance values of both SiNTs and GeNTs were drastically reduced over the studied wavelength as their $L$ increased. The hemispherical reflectance can be reduced to ~1% (Figure 5c,d), taking the absorption to 99% (Figure 5e,f) over the UV–vis spectrum for ~1.1 $\mu$m long SiNTs and ~1.7 $\mu$m long GeNTs.

The variation of $R$% and $A$%, at 500 nm, of the SiNTs and GeNTs, as a function of their lengths is shown in Figure 5g,h. Figure 5g shows the total hemispherical reflectance of SiNTs drastically decreasing from 40 to

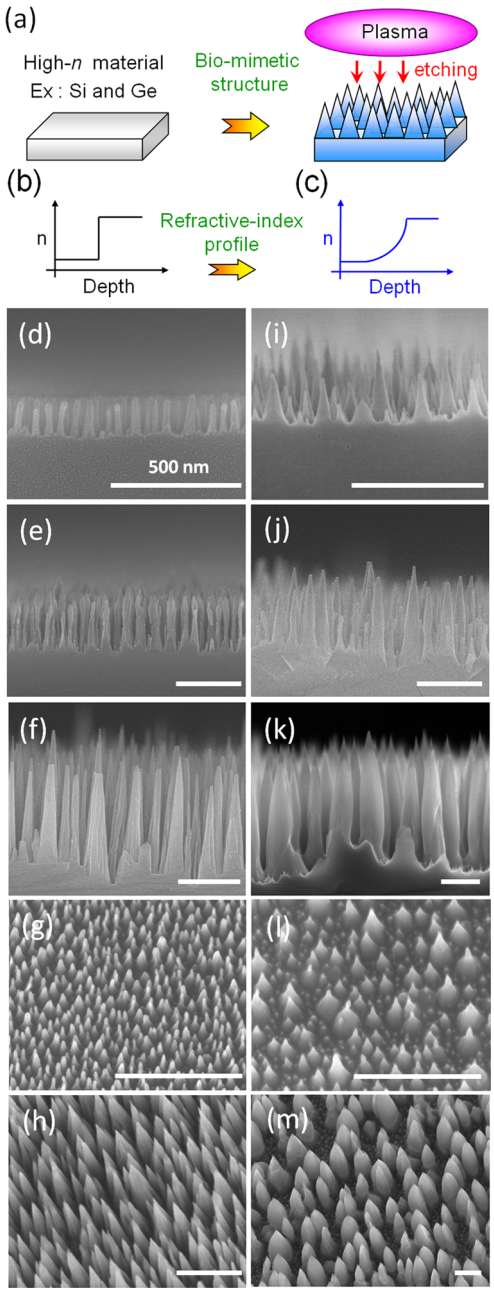


**Figure 4. Fabrication of cicada mimetic nanotip arrays. (a) Schematic illustration of the fabrication procedure for bioinspired nanostructures on high-index semiconductor substrates (Si and Ge) using a self-masked dry etching method. Schematic showing the effective refractive index profile of the (b) polished substrate (ungraded) and the (c) cicada wing-like nanostructured (graded) substrate. SEM images of Cicada mimetic (d–h) SiNTs and (i–m) GeNTs. Cross-section SEM images of SiNTs with $L$ = (d) 138, (e) 465, and (f) 1175 nm. Tilted top view SEM images of SiNTs with $L$= (g) 138 and (h) 1175 nm. Cross-section SEM images of GeNTs with $L$ = (i) 230, (j) 625, and (k) 1750 nm. Tilted top view SEM images of GeNTs with $L$ = (l) 230 and (m) 1750 nm. Scale bar = 500 nm (d–m).**

~1% and total hemispherical absorption significantly increasing from 60 to ~99% when the length increases to 1.1 $\mu$m. For GeNTs, the total hemispherical reflectance decreased from ~50 to ~1% and absorption

**TABLE 1. Geometrical Features of Different Nanotip Arrays**

| nanotip array | $L$ (nm) | $d$ (nm) | $S$ (nm) |
|---|---|---|---|
| short SiNT (Figure 4d,g) | 138 ± 11 | 35 ± 8 | 56 ± 15 |
| medium SiNT (Figure 4e) | 465 ± 28 | 66 ± 15 | 90 ± 27 |
| long SiNT (Figure 4f,h) | 1175 ± 53 | 175 ± 30 | 205 ± 50 |
| short GeNT (Figure 4i,l) | 230 ± 48 | 80 ± 9 | 60 ± 30 |
| medium GeNT (Figure 4j) | 625 ± 56 | 115 ± 20 | 125 ± 24 |
| long GeNT (Figure 4k,m) | 1750 ± 101 | 320 ± 45 | 320 ± 74 |

increased up to 99% as the length increased to 1.7 $\mu$m (Figure 5h). However, the hemispherical absorption of SiNTs and GeNTs will slightly decrease in the NIR region due to the decrease in the absorbed component of the light below the band gap of Si (1.12 eV) and Ge (0.66 eV), as shown in Figure 5e,f. A 2D color-coded theoretical plot of the $R$% as a function of $L/S$ and $S/\lambda$ is shown for SiNTs (Figure 5i) and GeNTs (Figure 5j), showing a blue area where the target reflectance was achieved. In these plots, experimentally measured data from real samples, three each from SiNTs and GeNTS, were inserted (black symbols). The measured (actual) and predicted (calculated) $R$ values for these samples were consistent and commensurate (Supporting Information Table S1).

Having proved the validity of the theoretical predictions for broad-band AR properties in the SiNTs and GeNTs, the final confirmation was expected from the AOI-dependent studies. Figure 6 shows the AR properties of actual high-index SiNT and GeNT substrates. The specular reflectance data for SiNTs (Figure 6a,b) and GeNTs (Figure 6c,d) show the efficacy of the Cicada mimetic NT structures in suppressing the reflectance over a wide range of AOI in comparison to the planar surfaces under 632.8 nm incident light. The experimentally measured results of angular reflectance for SiNTs correspond well with the calculated data (Figure 3).

Finally, in Figure 6e−h, we compare both the broad-band and omnidirectional attributes of reflectance and absorptance spectra for SiNTs (Figure 6e,f) and GeNTs (Figure 6g,h) vis-à-vis their planar counterparts. The results indicate that near unity absorption ($A \sim 99\%$) could be achieved over 400−1200 nm and AOI from 0 to 60° for Cicada mimetic NTs of Si and Ge having prescribed lengths and spacing as designed from FDTD simulations. To the best of our knowledge, such excellent omnidirectional absorption properties have not been achieved.[44]

## DISCUSSION

In most cases, natural designs prove to be the most efficient for a given functionality. Without being extravagant, nature imparts just enough functionality to her designs to suit the purpose. The moth eye, for example, expresses good AR properties only over the visible band but not over the infrared or above which is useless for the insect. This way the efficiency of the design is maintained. AR structures which are used in solar cells and photodetectors would also benefit if we learn from nature and customize the design according to the particular application. The Cicada wing design, a 250 nm structure demonstrating around 1% reflectance in the visible band, which we have followed here, should be enough for the target applications. Thus, we have set ourselves a target reflectance of 1% over the visible band for most of the light-harvesting applications. Such targets are in fact enough to ensure functionally viable products.

After studying the Cicada wing structure (Figure 1), we constructed a theoretical model of the natural system and obtained optical properties of the model theoretically using FDTD. These included calculation of the reflectance/absorption over a broad-band wavelength (Figure 2) and wide AOI (Figure 3) in the biomimetic structures. However, to prepare a design rule, specific morphology dimensions have to be proposed which should be experimentally applicable to key materials being used in the target industry and provide a logical design route for the rest. Hence, the calculated $R$% should be mapped over physical dimensions $L$ and $S$ of the biomimetic structure and then extended to other materials of different RI.

The interplay of $L$ and $S$ of the natural structure with the select band of optical wavelength led us to categorize $L/S$ and $S/\lambda$ as the two most important geometrical parameters that would tune the reflectance. The AR effect demonstrated in these NT structures is generally explained on the basis of GRIN.[1,45] GRIN relies on the exact RI of the media, a mixture of air and solid material with a certain volume fraction, at each $XY$ plane over the whole length (along $Z$) of the structure.[1,45] A smoother gradient of RI, to suppress the reflectance, would require longer nanostructures for high-index materials, but shorter nanostructures would do for a low-index material.[1] Different theoretical gradients have been proposed to suppress reflectance more efficiently, but a simple GRIN profile as published before[1,38,39] is safe to assume for the Cicada wing morphology.

The FDTD calculations predict that for small RI materials ($SiO_2$, ITO) lower values of $L/S$ are enough to achieve the 1% reflectance. For materials with larger RI values, such as Si and Ge, higher $L/S$ values are required. These results are the outcome of the GRIN principle applied specifically for the tip structure. Briefly, a smaller effective index at the air−material interface would ensure smaller $R$%. Assuming air ($n$ = 1.0) as the surrounding medium, the effective index for the tip structure, calculated by Bruggeman's approximation, requires smaller length for a smoother gradient with material having RI closer to that of air, that is, low RI materials. However, for higher RI material (such

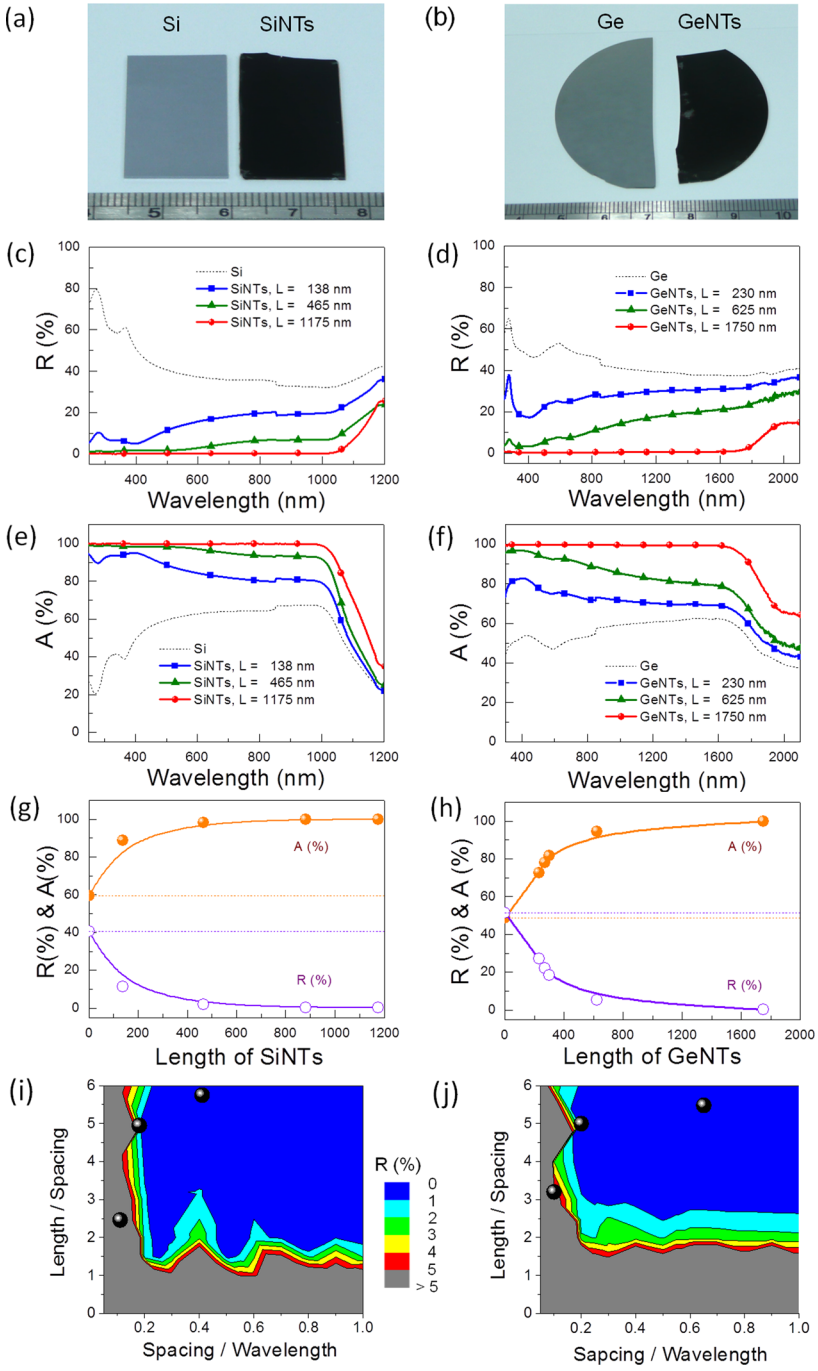


**Figure 5. Broad-band absorption of black SiNTs and GeNTs. Photographic image of planar (left) and nanostructured (right) surfaces of (a) Si and (b) Ge. Lengths of the SiNTs and GeNTs were 1175 and 1750 nm, respectively. Comparison of the total hemispherical (c,d) reflectance and (e,f) hemispherical absorption spectrum as a function of wavelength for a polished wafer (black dashed line) and different lengths of nanotips (colored solid line) of Si (left column) and Ge (right column), respectively. Total reflectance (hollow circle) and absorption (solid circle) measured at a specific wavelength of 500 nm as a function of the nanotip lengths: (g) SiNTs and (h) GeNTs. Dashed lines (in g,h) indicate the total reflectance and absorption values (at 500 nm) for the planar polished wafer as reference. The solid lines connecting the data points are a guide to the eye only. The 2D contour reflectance, at 500 nm, map as a function of $L/S$ and $S/\lambda$ for (i) SiNTs and (j) GeNTs. Gradient spectral colors from red to blue represent the reflectance value from 5 to 0% for the nanotip arrays. Gray color represents a reflectance value >5%. The black data points represent geometrical parameters for real SiNTs and GeNTs, as shown in the SEM image (Figure 4).**

as Si or Ge), the effective index is small only at a large $L$, where the material volume fraction is sufficiently small compared to air. Specific values for these parameters were then predicted for $SiO_2$, ITO, SiNT, and GeNT structures (Figures 2 and 3).

Following the prediction, nanostructures were fabricated on materials that could be used in the electron cyclotron resonance microwave plasma etching system, with physical dimensions matching the prescribed values as far as practicable (Figure 4).

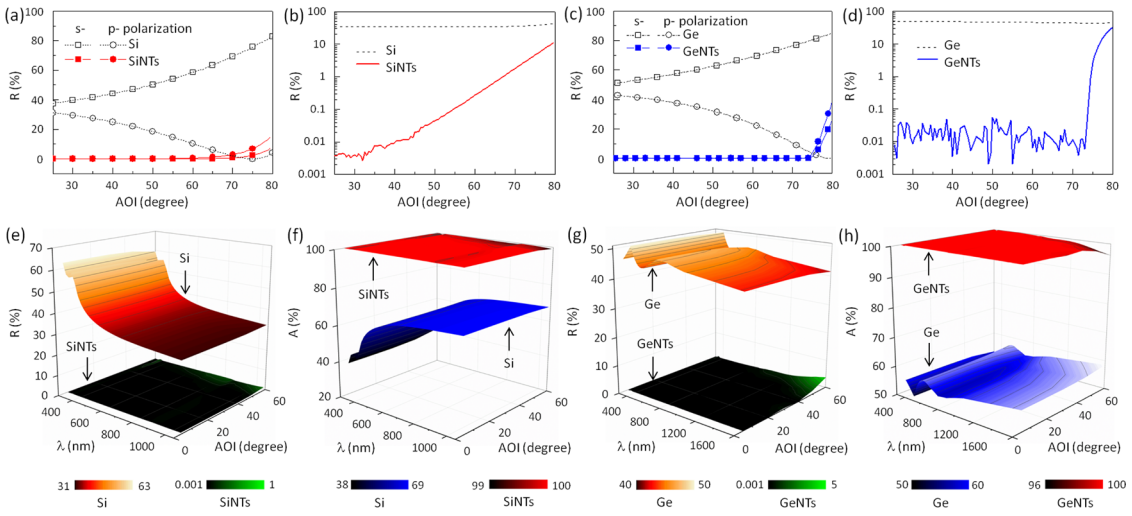


**Figure 6. Broad-band and omnidirectional optical properties of SiNTs and GeNTs. (a) Specular reflectance of the Si wafer and the SiNTs ($L$ = 1.4 $\mu$m) as a function of angle of incidence using (□) s- and (○) p-polarized light of 632.8 nm wavelength. (b) Specular reflectance for unpolarized light (random ∼ average of s- and p-polarized data), plotted on a logarithmic scale. (c) Specular reflectance of the Ge wafer and the GeNTs ($L$ = 1.75 $\mu$m) as a function of angle of incidence using (□) s- and (○) p-polarized light of 632.8 nm wavelength. (d) Specular reflectance for unpolarized light (random ∼ average of s- and p-polarized data), plotted on a logarithmic scale. The 3D plot of $R$% and $A$% as a function of wavelength and AOI for (e,f) Si wafer and SiNT and (g,h) Ge wafer and GeNTs using unpolarized light.**

Etching time predominantly controlled the length of the array, and process gas ($CH_4$, $SiH_4$, Ar, $H_2$) ratios, especially $CH_4$:$SiH_4$, could be adjusted to control the spacing. Morphology control of the nanotip arrays has been reported before.[43] Plasma-based fabrication and control of such tip-like structures,[42] especially the short ones, is challenging and can only be accomplished with proper understanding of the physical−chemical processes going on in the plasma.[46] In this case, SiNTs ($L$ = 1.4 $\mu$m) and GeNTs ($L$ = 1.75 $\mu$m) were produced with prescribed dimensions. Satisfactory visual inspection (Figure 5a,b) compelled us to measure the detailed broad-band reflectance property. The measured set of data was then compared with the predicted results (Supporting Information Table S1) and was found to be acceptable. This indicated the accuracy of the model and the procedures being followed. The observed deviations in the predicted and measured reflectance values (Supporting Information Table S1) may be due to the size ($L$ and $S$) distribution of the experimentally fabricated random and aperiodic NTs, whereas the calculations assumed no distribution of the $L$ and $S$ values.

On the oxide materials, such as ITO and $SiO_2$, long NT structures could not be made because of the lack of preferred etching planes and a slow plasma etching rate. Our trials on oxides and metals resulted in extremely short, rounded apex structures without much control over its length and spacing.[34] In fact, researchers prefer bottom-up growth for ITO-based antireflection coatings.[47] As a result of such lack of instrumental facilities or process incompatibility, an extrapolation was used. For example, we compared the real data of the Cicada wing with a model $SiO_2$ NT structure having dimensions similar to that of the Cicada wing (Supporting Information Table S1). We have assumed similar RI for $SiO_2$ and chitin (Cicada wing) (Supporting Information Figure S1). The predicted and actual $R$% results were similar.

The same methodology was adopted for the AOI dependence of the reflectance data. We compared the calculated (Figure 3) and measured spectra (Figure 6a−d) and obtained close similarity between the two. Finally, the SiNTs and GeNTs with 1.4 and 1.75 $\mu$m length, respectively, were shown to offer near unity absorption over the visible band and sufficiently wide AOI of 60°. The validity of the calculation on Si and Ge and close match of the $SiO_2$ calculation with the Cicada wing structure give credibility to our model and the proposed design principles. Extensive mapping of the RI space could be carried out depending on the particular production to achieve cost savings by this analysis.

Lastly, we remind the readers that the results presented above must be considered under some general assumptions. First, we assumed perfectly aligned, cone-shaped, closely packed NTs in a square lattice for our FDTD simulation (Figure S1). The results also indicate that the rate of reflectance reduction is significant within the initial several hundreds of nanometers in length of the nanostructures. The rate of reflectance decay is limited and ultimately flattens at longer lengths. This follows the theoretical predictions of graded-index pyramidal surfaces.[1,45,48] We did not include other geometrical factors, such as tapering angle, paraboloid/Gaussian surface,[49] random nanowires,[50] low-$n$ ($n$ < 1) materials,[51] or negative RI effects.[52]

## CONCLUSION

Broad-band and omnidirectional antireflection properties of Cicada-inspired nanostructures have been studied theoretically (FDTD) and experimentally in materials of photovoltaic significance. Geometrical parameters, length/spacing ($L/S$) and spacing/wavelength ($S/\lambda$), were tuned to create a zone of optimum target reflectance of 1% in the 300−1000 nm region, as demonstrated by the Cicada. The minimum values of $L/S$ and $S/\lambda$ to enter this zone serve as a design rule for the production process aiming at technical viability and cost competitiveness. Smaller values of $L/S$ and $S/\lambda$ are required for materials with low refractive indices ($SiO_2$, ITO) compared to Si or Ge at the high end of the scale. The theoretical model has been verified by using experimental data from plasma-etched real biomimetic Si and Ge nanotip surfaces. A design rule, $L \sim 1.5\ \mu$m and $S \sim 200$ nm in high RI Si and Ge substrates and $L \sim 200-600$ nm and $S \sim 100-400$ nm in low RI $SiO_2$ or ITO, has been proposed which could be followed in different light-harvesting materials that would exhibit ~99% optical absorption. This design rule is applicable over the visible band and at least up to and angle of incidence of 60° for material RI spanning 1.5−4.

## METHODS

**Sample Preparation.** Single-crystalline (100) n-type silicon and germanium wafers, single side polished, were cleaned with acetone, methanol, and deionized water prior to the fabrication process. Uniform arrays of Si and Ge nanostructure arrays were created by a high-density electron cyclotron resonance plasma etching using a gas mixture of silane ($SiH_4$), methane ($CH_4$), hydrogen ($H_2$), and argon (Ar). A detailed description of the nanostructure array formation by the self-masked dry etching technique can be found elsewhere.[15,42,43] The plasma etching time controlled the length of the nanostructures from ~150 to ~1800 nm, and gas flow ratios primarily controlled the spacing. Similar plasma etching methods have been adopted by other researchers also.[26,46]

**Morphology.** Observation of the surface morphology and dimension measurement of the Cicada wings and the semiconductor nanostructures were done with a JEOL 6700 field-emission scanning electron microscope.

**Optical Measurements.** The total reflectance ($R$%), transmittance ($T$%), and absorption ($A$% = 100% − $R$% − $T$%) of the nanostructures and the Cicada wing were measured using a JASCO-V 670 (UV−vis−NIR) spectrophotometer attached with an integrating sphere. A 250−2100 nm range of wavelength was scanned in the spectrophotometer that uses a change in light source at 350 nm and a change of grating at 850 nm. A sample size of 1.0 × 1.5 $cm^2$ was used for the measurement.

A stabilized helium−neon laser (632.8 nm) with frequency stability of ±5 MHz was used to measure the reflectance−incident angle spectrum (25−80°). The angular resolution of the instrument was 0.01°. The specular angular reflectance as a function of wavelength (250−1600 nm) and various angles of incidence (5−60°) were measured with a JASCO ARN-475 spectral measurement accessory.

**Finite Difference Time Domain Simulations.** For the calculation of the broad-band antireflection characteristics, we used the commercially available Lumerical[53] software for three-dimensional FDTD calculations. The 3D nanotip arrays (Supporting Information Figure S1a), resembling the Cicada wing structure, were used for this optical simulation. The unit cell for the FDTD simulation uses geometrical parameters of length ($L$) and spacing ($S$) of the nanotips. We have applied the periodic, periodic, and perfectly matched layer boundary conditions for normal incidence along the orthogonal $x$-, $y$-, and $z$-boundaries of the unit cell, as shown in Supporting Information Figure S1b. The $z$-axis is along a plane wave where light is propagating and incident on the structure; the electric field ($E$) polarization is along the $x$-axis, and the $y$-axis is directed perpendicular and out of the plane of the paper. The wavelength-dependent real ($n$) and imaginary ($k$) part of the RI for low- ($SiO_2$), medium- (indium tin oxide), and high-index substrate materials (Si and Ge) were taken from Palik,[41] and a background RI of 1.0 (air) was assumed Figure S1 (c−e). A detailed description of the far-field optical simulation conditions, using FDTD, can be found elsewhere.[40]

*Conflict of Interest:* The authors declare no competing financial interest.

*Acknowledgment.* The authors wish to thank the National Science Council, Taiwan, under Grant No. NSC-101-2112-M-010-003-MY3 for the financial support.

*Supporting Information Available:* FDTD simulation model for Cicada mimetic nanotip arrays, calculated reflection mapping on Cicada mimetic nanotip arrays by FDTD simulation, calculated wide-angle antireflection property of Cicada mimetic silicon, silica, ITO, and Ge nanotip arrays, and a table of comparison of FDTD predicted and actual measured $R$% values in index-controlled nanostructures with different feature parameters. This material is available free of charge *via* the Internet at http://pubs.acs.org.

## REFERENCES AND NOTES

1. Chattopadhyay, S.; Huang, Y. F.; Jen, Y. J.; Ganguly, A.; Chen, K. H.; Chen, L. C. Anti-reflecting and Photonic Nanostructures. *Mater. Sci. Eng. Rep.* **2010**, *69*, 1–35.
2. Brongersma, M. L.; Cui, Y.; Fan, S. Light Management for Photovoltaics Using High-Index Nanostructures. *Nat. Mater.* **2014**, *13*, 451–460.
3. Boettcher, S. W.; Spurgeon, J. M.; Putnam, M. C.; Warren, E. L.; Turner-Evans, D. B.; Kelzenberg, M. D.; Maiolo, J. R.; Atwater, H. A.; Lewis, N. S. Energy-Conversion Properties of Vapor−Liquid−Solid-Grown Silicon Wire-Array Photocathodes. *Science* **2010**, *327*, 185–187.
4. Bae, J.; Kim, H.; Zhang, X. M.; Dang, C. H.; Zhang, Y.; Choi, Y. J.; Nurmikko, A.; Wang, Z. L. Si Nanowire Metal−Insulator−Semiconductor Photodetectors as Efficient Light Harvesters. *Nanotechnology* **2010**, *21*, 095502–5.
5. Wallentin, J.; Anttu, N.; Asoli, D.; Huffman, M.; Åberg, I.; Magnusson, M. H.; Siefer, G.; Fuss-Kailuweit, P.; Dimroth, F.; Witzigmann, B.; et al. InP Nanowire Array Solar Cells Achieving 13.8% Efficiency by Exceeding the Ray Optics Limit. *Science* **2013**, *339*, 1057–1060.
6. Graydon, O. Perfect Absorber. *Nat. Photonics* **2014**, *8*, 2.
7. Nefedov, I. S.; Valaginnopoulos, C. A.; Melnikov, L. A. Perfect Absorption in Graphene Multilayers. *J. Opt.* **2013**, *15*, 114003.
8. Atwater, H. A.; Polman, A. Plasmonics for Improved Photovoltaic Devices. *Nat. Mater.* **2010**, *9*, 205–213.
9. Chen, H. T.; Zhou, J.; O'Hara, J. F.; Chen, F.; Azad, A. K.; Taylor, A. J. Antireflection Coating Using Metamaterials and Identification of Its Mechanism. *Phys. Rev. Lett.* **2010**, *105*, 073901.
10. Aydin, K.; Ferry, V. E.; Briggs, R. M.; Atwater, H. A. Broadband Polarization-Independent Resonant Light Absorption Using Ultrathin Plasmonic Super Absorbers. *Nat. Commun.* **2011**, *2*, 517.
11. Pala, R. A.; Liu, J. S. Q.; Barnard, E. S.; Askarov, D.; Garnett, E. C.; Fan, S.; Brongersma, M. L. Optimization of Non-periodic

Plasmonic Light Trapping Layers for Thin-Film Solar Cells. *Nat. Commun.* **2013**, *4*, 2095–2097.
12. Yang, Z. P.; Ci, L.; Bur, J. A.; Lin, S. Y.; Ajayan, P. M. Experimental Observation of an Extremely Dark Material Made by a Low-Density Nanotube array. *Nano Lett.* **2008**, *8*, 446–451.
13. Mizunoa, K.; Ishiib, J.; Kishidac, H.; Hayamizua, Y.; Yasudaa, S.; Futabaa, D. N.; Yumuraa, M.; Hataa, K. A Black Body Absorber from Vertically Aligned Single-Walled Carbon Nanotubes. *Proc. Natl. Acad. Sci. U.S.A.* **2009**, *106*, 6044–6047.
14. Xi, J. Q.; Schubert, M. F.; Kim, J. K.; Schubert, E. F.; Chen, M.; Lin, S. Y.; Liu, W.; Smart, J. A. Optical Thin-Film Materials with Low Refractive Index for Broadband Elimination of Fresnel Reflection. *Nat. Photonics* **2007**, *1*, 176–179.
15. Huang, Y. F.; Chattopadhyay, S.; Jen, Y. J.; Peng, C. Y.; Liu, T. A.; Hsu, Y. K.; Pan, C. L.; Lo, H. C.; Hsu, C. H.; Chang, Y. H.; et al. Improved Broadband and Quasi Omnidirectional Anti-reflection Properties with Biomimetic Silicon Nanostructures. *Nat. Nanotechnol.* **2007**, *2*, 770–774.
16. Spinelli, P.; Verschuuren, M. A.; Polman, A. Broadband Omnidirectional Antireflection Coating Based on Subwavelength Surface Mie Resonators. *Nat. Commun.* **2012**, *3*, 692–695.
17. Macleod, H. A. *Thin-Film Optical Filters*, 4th ed.; CRC Press: Boca Raton, FL, 2010.
18. Parker, A. R.; Townley, H. E. Biomimetics of Photonic Nanostructures. *Nat. Nanotechnol.* **2007**, *2*, 347–353.
19. Editorial. Nature's Guiding Light. *Nat. Photonics* **2008**, *2*, 639.
20. Kumar, C. S. S. R. *Biomimetic and Bioinspired Nanomaterials*; Wiley-VCH: Weinheim, Germany, 2010.
21. Chen, J. D.; Zhou, L.; Ou, Q. D.; Li, Y. Q.; Shen, S.; Lee, S. T.; Tang, J. X. Enhanced Light Harvesting in Organic Solar Cells Featuring a Biomimetic Active Layer and a Self-Cleaning Antireflective Coating. *Adv. Energy Mater.* **2014**, *4*, 1301777.
22. Leem, J. W.; Kim, S.; Lee, S. H.; Rogers, J. A.; Kim, E.; Yu, J. S. Efficiency Enhancement of Organic Solar Cells Using Hydrophobic Antireflective Inverted Moth-Eye Nanopatterned PDMS Films. *Adv. Energy Mater.* **2014**, *4*, 1301315.
23. Lou, S.; Guo, X.; Fan, T.; Zhang, D. Butterflies—Inspiration for Solar Cells and Sunlight Water-Splitting Catalysts. *Energy Environ. Sci.* **2012**, *5*, 9195–9216.
24. Seo, M. L.; Woo, J. H.; Lee, D.; Im, H.; Hur, J.; Choi, Y. K. Nature-Replicated Nano-in-Micro Structures for Triboelectric Energy Harvesting. *Small* **2014**, *10*, 3887–3894.
25. Bae, J.; Kim, H.; Zhang, X. M.; Dang, C. H.; Zhang, Y.; Choi, Y. J.; Nurmikko, A.; Wang, Z. L. Si Nanowire Metal–Insulator–Semiconductor Photodetectors as Efficient Light Harvesters. *Nanotechnology* **2010**, *21*, 095502–5.
26. Ivanova, E. P.; Hasan, J.; Webb, H. K.; Gervinskas, G.; Juodkazis, S.; Truong, V. K.; Wu, A. H. F.; Lamb, R. N.; Baulin, V. A.; Watson, G. S.; et al. Bactericidal Activity of Black Silicon. *Nat. Commun.* **2013**, *4*, 2838.
27. Parker, A. R. *Optical Biomimetics: Materials and Applications*; Woodhouse Publishing Co.: Cambridge, UK, 2012.
28. Raut, H. K.; Ganesh, V. A.; Nair, A. S.; Ramakrishna, S. Antireflective Coatings: A Critical, In-Depth Review. *Energy Environ. Sci.* **2011**, *4*, 3779–3804.
29. Li, Y.; Zhang, J.; Yang, B. Antireflective Surfaces Based on Biomimetic Nanopillared Arrays. *Nano Today* **2010**, *5*, 117–127.
30. Wu, H. M.; Lai, C. M.; Peng, L. H. Optical Response From Lens-like Semiconductor Nipple Arrays. *Appl. Phys. Lett.* **2008**, *93*, 211903.
31. Sobahan, K. M. A.; Park, Y. J.; Kim, J. J.; Hwangbo, C. K. Nanostructured Porous $SiO_2$ Films for Antireflection Coatings. *Opt. Commun.* **2011**, *285*, 873–876.
32. Ehret, G.; Buhr, E.; Gäbler, S.; Bitzer, H. M. Broadband Optical Antireflection of Plastic Optics by Molded Stochastic Sub-wavelength Structures. *Plasma Process. Polym.* **2009**, *6*, 840–847.
33. Bernhard, C. G.; Miller, W. H. A Corneal Nipple Pattern in Insect Compound Eyes. *Acta Physiol. Scand.* **1962**, *56*, 385–386.
34. Yoshida, A.; Motoyama, M.; Kosaku, A.; Miyamoto, K. Nanoprotuberance Array in the Transparent Wing of a Hawkmoth, *Cephonodes hylas*. *Zool. Sci.* **1996**, *13*, 525–526.
35. Choi, K.; Park, S. H.; Song, Y. H.; Lee, Y. T.; Hwangbo, C. K.; Yang, H.; Lee, H. S. Nano-tailoring the Surface Structure for the Monolithic High-Performance Antireflection Polymer Film. *Adv. Mater.* **2010**, *22*, 3713–3718.
36. Park, H.; Shin, D.; Kang, G.; Baek, S.; Kim, K.; Padilla, W. J. Broadband Optical Antireflection Enhancement by Integrating Antireflective Nanoislands with Silicon Nanoconical-Frustum Arrays. *Adv. Mater.* **2011**, *23*, 5796–5800.
37. Yoshida, A.; Motoyama, M.; Kosaku, A.; Miyamoto, K. Antireflective Nanoprotuberance Array in the Transparent Wing of a Hawkmoth, *Cephonodes hylas*. *Zool. Sci.* **1997**, *14*, 737–741.
38. Clapham, P. B.; Hutley, M. C. Reduction of Lens Reflexion by the "Moth Eye" Principle. *Nature* **1973**, *244*, 281–282.
39. Wilson, S. J.; Hutley, M. C. The Optical Properties of Moth Eye Antireflection Surfaces. *J. Mod. Opt.* **1982**, *29*, 993–1009.
40. Huang, Y. F.; Chattopadhyay, S. Nanostructure Surface Design for Broadband and Angle-Independent Antireflection. *J. Nanophotonics* **2012**, *7*, 073594.
41. Palik, E. D. *Handbook of Optical Constants of Solids III*; Academic Press: New York, 1997.
42. Hsu, C. H.; Lo, H. C.; Chen, C. F.; Wu, C. T.; Hwang, J. S.; Das, D.; Tsai, J.; Chen, L. C.; Chen, K. H. Generally Applicable Self-Masked Dry Etching Technique for Nanotip Array Fabrication. *Nano Lett.* **2004**, *4*, 471–475.
43. Hsu, C. H.; Huang, Y. F.; Chen, L. C.; Chattopadhyay, S.; Chen, K. H.; Lo, H. C.; Chen, C. F. Morphology Control of Silicon Nanotips Fabricated by Electron Cyclotron Resonance Plasma Etching. *J. Vac. Sci. Technol., B* **2006**, *24*, 308–311.
44. Leem, J. W.; Song, Y. M.; Yu, J. S. Broadband Antireflective Germanium Surfaces Based on Subwavelength Structures for Photovoltaic Cell Applications. *Opt. Express* **2011**, *19*, 26308–26317.
45. Southwell, W. H. Pyramid-Array Surface-Relief Structures Producing Antireflection Index Matching on Optical Surfaces. *J. Opt. Soc. Am.* **1991**, *8*, 549–553.
46. Ostrikov, K.; Neyts, E. C.; Meyyappan, M. Plasma Nanoscience: From Nano-Solids in Plasmas to Nano-Plasmas in Solids. *Adv. Phys.* **2013**, *62*, 113–224.
47. O'Dwyer, C.; Szachowicz, M.; Visimberga, G.; Lavayen, V.; Newcomb, S. B.; Sotomayor Torres, C. M. Bottom-Up Growth of Fully Transparent Contact Layers of Indium Tin Oxide Nanowires for Light-Emitting Devices. *Nat. Nanotechnol.* **2009**, *4*, 239–244.
48. Deinega, A.; Valuev, I.; Potapkin, B.; Lozovik, Y. Antireflective Properties of Pyramidally Textured Surfaces. *Opt. Lett.* **2010**, *35*, 106–108.
49. Song, Y. M.; Jang, S. J.; Yu, J. S.; Lee, Y. T. Bioinspired Parabola Subwavelength Structures for Improved Broadband Antireflection. *Small* **2010**, *6*, 984–987.
50. Du, Q. G.; Kam, C. H.; Demir, H. V.; Yu, H. Y.; Sun, X. W. Broadband Absorption Enhancement in Randomly Positioned Silicon Nanowire Arrays for Solar Cell Applications. *Opt. Lett.* **2011**, *36*, 1884–1886.
51. Chen, H. Y.; Lin, H. W.; Wu, C. Y.; Chen, W. C.; Chen, J. S.; Gwo, S. Gallium Nitride Nanorod Arrays as Low-Refractive-Index Transparent Media in the Entire Visible Spectral Region. *Opt. Express* **2008**, *16*, 8106–8116.
52. Monzón, J. J.; Barriuso, A. G.; Sánchez-Soto, L. L. Perfect Antireflection *via* Negative Refraction. *Phys. Lett. A* **2006**, *349*, 281–284.
53. http://www.lumerical.com/.